IEEE Access
Multidisciplinary ⋮ Rapid Review ⋮ Open Access Journal

Received 16 June 2024, accepted 30 June 2024, date of publication 3 July 2024, date of current version 12 July 2024.

*Digital Object Identifier 10.1109/ACCESS.2024.3422846*

RESEARCH ARTICLE

# Tri-/Quad-/Quint-Band Bandpass Filters Based on Transversal Embedded Asymmetrical Square-Ring Resonator

**XIAOHAN WAN, ZHENGZHEN JIN, YIFAN WANG, GUOXIN XU, LEI ZHANG, YANG XIONG, AND LITIAN WANG**

Tianjin Key Laboratory of Film Electronic and Communication Devices, School of Integrated Circuit Science and Engineering, Tianjin University of Technology, Tianjin 300384, China

Corresponding author: Litian Wang (wanglitianrf@sina.com)

This work was supported in part by Guangzhou Key Research and Development Program, Major Science and Technology Projects, under Grant 202206070001; and in part by the Natural Science Foundation of Tianjin under Grant 23YDTPJC00600.

**ABSTRACT** This paper presents a series design method for tri-/quad-/and quint band bandpass filter (BPF) with multiple transmission zeros (TZs) based on an embedded asymmetrical square-ring resonator (ASRR). Firstly, we proposed a series of tri-/quad-/and quint-mode asymmetrical square-ring resonators which resonant modes are demonstrated by employing the multi-path matrix coupling analysis method. Further, we nested two identical ASRRs to construct multiple passbands and introduced multiple transmission zeros between frequency bands based on transversal signal interference concepts. Finally, tri-/quad-/quint-band BPFs are designed according to the proposed design principle using the proposed typical basic structure ASRR. The design, fabrication, and measurement of the three BPFs are conducted to validate their feasibility. The measured results consistently match the theoretical predictions, demonstrating superior performance, such as independent and controllable frequency band characteristics and abundant transmission zeros, while having promising potential to further expand frequency band designs.

**INDEX TERMS** Square-ring, asymmetrical, transversal signal interaction, independence manageable passband.

## I. INTRODUCTION

With the increasing competition for spectrum resources in modern communication networks and the widespread reuse of core frequency bands. There is a rapidly growing demand for multiple passbands for the sub-2.4 GHz basic coverage band and the 5G application trend. Therefore, the design and implementation of multi-band filters have become a research hotspot in recent years. As a critical key building block in multi-service communication systems, multiple-band bandpass filters (BPF) have aroused much attention and are widely investigated, so two major design methods of multiple-band BPFs are proposed.

To construct multiple-band BPFs, as one of the popular methods, combining filters was directly employed to achieve this design requirement [1], [2], [3], [4], [5], [6], [7]. For this cascade designing methodology, a series of BPFs based on a simple structure was employed to create a complex multi-band filter [1], [2], [3], [4]. The multi-band BPFs designed by paralleled multi-mode resonators were demonstrated in [5], [6], and [7], which BPFs are of common output port and input port. However, either cascade or parallel methodologies with the flaw of relatively large circuit size and complex architecture.

Recently, to further miniaturize the size of multiple-band BPFs, the BPFs based on the multimode resonator design were proposed [8], [9], [10], [11], [12], [13], [14], [15], [16], [17], [18], [19], [20], [21], [22], [23]. By adopting the square ring resonator, the multi-band BPF with sharp passband shirts and miniaturized circuit size could be achieved [8], [9], [10], [11]. To further address the issue of complex architecture, the Stepped Impedance resonators (SIR) [12], [13],

The associate editor coordinating the review of this manuscript and approving it for publication was Bilal Khawaja.


**FIGURE 1.** (a) Basic structure Tri-ASRR. (b) Transmission line model of Tri-ASRR.

[14], [15], [16], [17] were proposed. However, with this approach, the implementation of independent and controllable frequency band characteristics could be a challenge. Moreover, multiple-band BPF with independent controllable passband could be obtained by constructing multiple cross-coupling [18], [19], [20], [21], [22], [23]. Nevertheless, to realize further expanded frequency band designs still needs to be further investigated. To the best of our acknowledged, there are seldom reports on quad-band and quint-band BPFs designs.

In this paper, a series of design methods for tri-/quad-/and quint-band bandpass filters are demonstrated and constructed based on the proposed novelty embedded asymmetrical square-ring resonator (ASRR). A detailed design method for multiple-band BPF with compact size, multiple transmission zeros (TZs) and independent manageable centred frequencies is given in this article. In addition, due to the introduction of the expanded asymmetrical square-ring, the proposed filter can easily realise quad-band, quint-band and even more frequency band designs for modern 5G applications. The prototype filter is designed, implemented, and tested to validate simulation analysis.

## II. TRI-BAND BPF ANALYSIS AND DESIGN

In this paper, a series of novel asymmetrical square-ring resonators with extendable architecture and additive resonant modes is presented. By adding asymmetrical stubs along the square-ring of the ASRR with a more controllable freedom multimode resonator is achieved. The proposed resonator structure with corresponding physical lengths and widths denoted by $L_{A1}$ to $L_{A4}$ and $W_a$, respectively. Due to its asymmetric structure, as depicted in Fig.1 (a), the proposed resonator no more adopts the classical odd and even mode analysis methods as traditional symmetric square ring resonators. To further demonstrate the characteristics of the proposed resonator, the Fig.1(b) sketches the ideal transmission line model (TLM) of ASRR. As shown in Fig. 1(b), $Y_{An}$ ($n$ = 1, 2, 3, and 4) and $\theta_{An}$ ($n$ = 1, 2, 3, and 4) represent the characteristic admittances and electrical lengths of counterpart micro-strip lines, respectively.

The electrical parameters of Tri-ASRR are in Fig.2. Herein, $Y_{ina}$ is the input admittance of Tri-ASRR with electrical parameters similar to Fig.1.(b). Moreover, the design methodology is demonstrated by using the ABCD matrix Y matrix accompanied with the $S$ matrix. For simplicity, $Y_{A1} = Y_{A2} = Y_{A3} = Y_{A4} = Y_a$ is assumed.

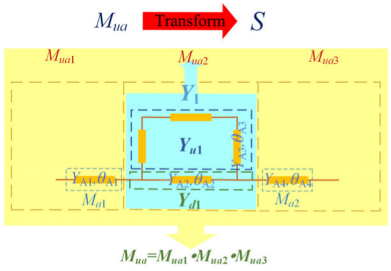


**FIGURE 2.** Equivalent ideal transmission line model for diagram analysis.

Since the ABCD matrix of microstrip line can be respectively defined as:

$$\begin{bmatrix} A & B \\ C & D \end{bmatrix} = \begin{bmatrix} \cos\theta & j\frac{1}{Y}\sin\theta \\ jY\sin\theta & \cos\theta \end{bmatrix} \tag{1}$$

where

$$M_{ua1} = M_{a1} = \begin{bmatrix} A & B \\ C & D \end{bmatrix}_{a1} = \begin{bmatrix} \cos\theta_{A1} & j\frac{1}{Y_a}\sin\theta_{A1} \\ jY_a\sin\theta_{A1} & \cos\theta_{A1} \end{bmatrix} \tag{2}$$

$$M_{ua3} = M_{a3} = \begin{bmatrix} A & B \\ C & D \end{bmatrix}_{a3} = \begin{bmatrix} \cos\theta_{A4} & j\frac{1}{Y_a}\sin\theta_{A4} \\ jY_a\sin\theta_{A4} & \cos\theta_{A4} \end{bmatrix} \tag{3}$$

The second part of the circuit is divided into the road and lower road, which belongs to the parallel network, using the Y matrix calculation from the definition:

$$M_{ua2} = [Y_1] = [Y_{u1}] + [Y_{d1}] \tag{4}$$

$$\begin{bmatrix} Y_{11} & Y_{12} \\ Y_{21} & Y_{22} \end{bmatrix} = \begin{bmatrix} \frac{D}{B} & \frac{-(AD-BC)}{B} \\ \frac{-1}{B} & \frac{A}{B} \end{bmatrix} \tag{5}$$

$$[Y_{11}]_{u1} = \frac{Y_a\cos(\theta_{A2}+2\theta_{A3})}{j\sin(\theta_{A2}+2\theta_{A3})} \tag{6}$$

$$[Y_{12}]_{u1} = \frac{-Y_a(\cos^2(\theta_{A2}+2\theta_{A3})+\sin^2(\theta_{A2}+2\theta_{A3}))}{j\sin(\theta_{A2}+2\theta_{A3})} \tag{7}$$

$$[Y_{21}]_{u1} = \frac{-Y_a}{j\sin(\theta_{A2}+2\theta_{A3})} \tag{8}$$

$$[Y_{22}]_{u1} = \frac{Y_a\cos\theta_{a2}}{j\sin(\theta_{A2}+2\theta_{A3})} \tag{9}$$

$$\begin{bmatrix} Y_{11} & Y_{12} \\ Y_{21} & Y_{22} \end{bmatrix}_{d1} = \begin{bmatrix} \frac{Y_a\cos\theta_{A2}}{j\sin\theta_{A2}} & \frac{-Y_a(\cos^2\theta_{A2}+\sin^2\theta_{A2})}{j\sin\theta_{A2}} \\ \frac{-Y_a}{j\sin\theta_{A2}} & \frac{Y_a\cos\theta_{A2}}{j\sin\theta_{A2}} \end{bmatrix} \tag{10}$$

For transmission $M_{ua2}$, the Y matrix can be expressed as follows:

$$[Y_{11}]_1 = \frac{Y_a\cos(\theta_{A2}+2\theta_{A3})}{j\sin(\theta_{A2}+2\theta_{A3})} + \frac{Y_a\cos\theta_{A2}}{j\sin\theta_{A2}} \tag{11}$$

$$[Y_{12}]_1 = \frac{-Y_a(\cos^2(\theta_{A2}+2\theta_{A3})+\sin^2(\theta_{A2}+2\theta_{A3}))}{j\sin(\theta_{A2}+2\theta_{A3})} + \frac{-Y_a(\cos^2\theta_{A2}+\sin^2\theta_{A2})}{j\sin\theta_{A2}} \tag{12}$$

$$[Y_{21}]_1 = \frac{-Y_a}{j\sin(\theta_{A2}+2\theta_{A3})} + \frac{-Y_a}{j\sin\theta_{A2}} \tag{13}$$

$$[Y_{22}]_1 = \frac{Y_a\cos(\theta_{A2}+2\theta_{A3})}{j\sin(\theta_{A2}+2\theta_{A3})} + \frac{Y_a\cos\theta_{A2}}{j\sin\theta_{A2}} \tag{14}$$

where the convert $Y$ matrix into the ABCD matrix is:

$$M_{ua2} = \begin{bmatrix} A & B \\ C & D \end{bmatrix}_{a2} = \begin{bmatrix} \frac{-Y_{11}}{Y_{21}} & \frac{-1}{Y_{21}} \\ \frac{-(Y_{11}Y_{22}-Y_{12}Y_{21})}{Y_{21}} & \frac{-Y_{11}}{Y_{21}} \end{bmatrix} = \frac{1}{Y_{21}}\begin{bmatrix} -Y_{22} & -1 \\ -(Y_{11}-Y_{22}) & -Y_{11} \end{bmatrix} \tag{15}$$

$$[A]_{a2} = \frac{\sin(\theta_{A2}+2\theta_{A3})\sin\theta_{A2}}{\sin(\theta_{A2}+2\theta_{A3})+\sin\theta_{A2}} \times \left(\frac{\cos(\theta_{A2}+2\theta_{A3})}{\sin(\theta_{A2}+2\theta_{A3})} + \frac{\cos\theta_{A2}}{\sin\theta_{A2}}\right) \tag{16}$$

$$[B]_{a2} = \frac{\sin(\theta_{A2}+2\theta_{A3})\sin\theta_{A2}}{\sin(\theta_{A2}+2\theta_{A3})+\sin\theta_{A2}} \tag{17}$$

$$[C]_{a2} = \frac{\sin(\theta_{A2}+2\theta_{A3})\sin\theta_{A2}}{\sin(\theta_{A2}+2\theta_{A3})+\sin\theta_{A2}} \times \frac{Y_a}{j}\left(\left(\frac{\cos(\theta_{A2}+2\theta_{A3})}{\sin(\theta_{A2}+2\theta_{A3})} + \frac{\cos\theta_{A2}}{\sin\theta_{A2}}\right)^2 - \left(\frac{-1}{\sin(\theta_{A2}+2\theta_{A3})} + \frac{-1}{\sin\theta_{A2}}\right)^2\right) \tag{18}$$

$$[D]_{a2} = \frac{\sin(\theta_{A2}+2\theta_{A3})\sin\theta_{A2}}{\sin(\theta_{A2}+2\theta_{A3})+\sin\theta_{A2}} \times \left(\frac{\cos(\theta_{A2}+2\theta_{A3})}{\sin(\theta_{A2}+2\theta_{A3})} + \frac{\cos\theta_{A2}}{\sin\theta_{A2}}\right) \tag{19}$$

Herein the ABCD matrix of Tri-ASRR can be expressed and derived by

$$M_{ua} = \begin{bmatrix} A & B \\ C & D \end{bmatrix}_1 = M_{ua1}\cdot M_{ua2}\cdot M_{ua3} \tag{20}$$

Consequently, the transmission coefficient and can be extracted separately as follows:

$$\begin{bmatrix} S_{11} & S_{12} \\ S_{21} & S_{21} \end{bmatrix} = \begin{bmatrix} \frac{A+BY_0-C/Y_0-D}{A+BY_0+C/Y_0+D} & \frac{2(AD-BC)}{A+BY_0+C/Y_0+D} \\ \frac{2}{A+BY_0+C/Y_0+D} & \frac{-A+BY_0-C/Y_0+D}{A+BY_0+C/Y_0+D} \end{bmatrix} \tag{21}$$

where $Y_0 = Y_{A1} = Y_{A2} = Y_{A3} = Y_{A4} = 0.01$S is the characteristic impedance of each segment of the microstrip line. For simplicity, $\theta_{A1} = \theta_{A4} = 2\theta_{A3} = 4\theta_{A2} = 120°$ are assumed. In order to find the input admittance, the ABCD matrix can be calculated as:

$$\begin{bmatrix} V_1 \\ I_1 \end{bmatrix} = \begin{bmatrix} A & B \\ C & D \end{bmatrix}\begin{bmatrix} V_2 \\ I_2 \end{bmatrix} \Rightarrow \begin{cases} V_{a1} = AV_{a2} + BI_{a2} \\ I_{a1} = CV_{a2} + DI_{a2} \end{cases} \tag{22}$$

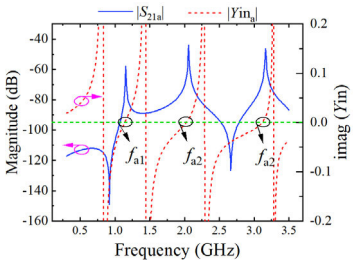


**FIGURE 3.** The imaginary part of input admittance $Y_{ina}$ of Tri-ASRR.

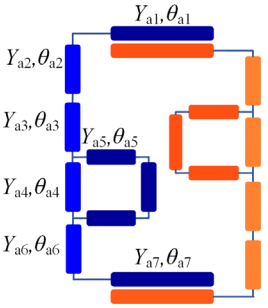


**FIGURE 4.** Equivalent ideal transmission line model of proposed Tri-band BPF.

Thus, the input admittance $Y_{\text{ina}}$ can be deduced from:

$$Y_{ina} = \frac{I_{a1}}{V_{a1}} = \frac{CV_{a2}+DI_{a2}}{AV_{a2}+BI_{a2}} = \frac{CZ_{aL}+D}{AZ_{aL}+B} \tag{23}$$

where:

$$Z_{aL} = V_{a2}/I_{a2} \tag{24}$$

$$Y_{ina} = \frac{C}{A} \tag{25}$$

According to resonant condition $\text{Im}(Y_{\text{ina}}) = 0$, the imaginary part of the input admittance in Tri-ASRR is plotted in Fig.3. It can be observed from Fig.3 that Tri-ASRR yields triple transmission poles $f_{a1}$, $f_{a2}$, and $f_{a3}$. Among them, $f_{a1}$ forms a group that falls within the range of the first desired frequency band, while $f_{a2}$ and $f_{a3}$ fall within the design range of the second and third frequency band, respectively. And the triple transmission poles of Tri-ASRR can be employed for the construction of the triple frequency bands.

The ideal TLM of Tri-band BPF is demonstrated in Fig.4, where the parameters $Y_{an}$ and $\theta_{an}$ ($n = 1, 2, 3, 4, 5, 6, 7$) represent the characteristic admittances and electrical lengths of the Tri-band BPF, respectively. Thus the Tri-ASRR can be employed to exploit a Tri-band BPF.

The phase shift of $S_{21}$ of Path A and Path A+Path B are respectively illustrated in Fig.5(a). As can be derived from Fig.5(a) that single Path A hardly generates any TZ. However, by utilizing the transversal signal interaction techniques of the dual transmission path from the input port to the output port, four extra transmission zeros ($TZ_{a1}$, $TZ_{a2}$, $TZ_{a3}$, $TZ_{a4}$) can be yielded. To further demonstrate the contribution mechanism of transmission zeros, which plot $TZ_{a2}$ and $TZ_{a3}$ versus $\theta_{a2}$

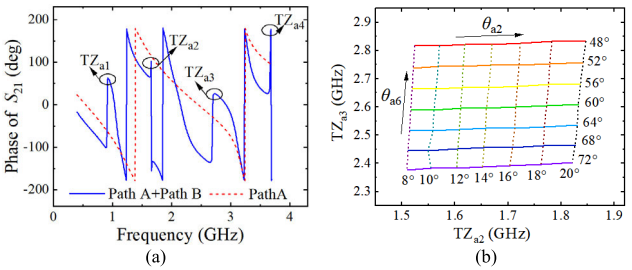


**FIGURE 5.** (a) Phase shift of $S_{21}$ Path A and Path B. (b)$TZ_{a2}$ and $TZ_{a3}$ versus varied $\theta_{a2}$ and $\theta_{a6}$.

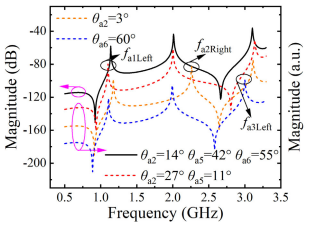


**FIGURE 6.** Transmission coefficient of triple varied conditions under weak coupling.

and $\theta_{a6}$ is shown in Fig.5(b). $TZ_{a2}$ increases with increasing $\theta_{a2}$, while $TZ_{a3}$ have little effect on $\theta_{a2}$. $TZ_{a3}$ shift down as $\theta_{a6}$ enlarges, whereas $TZ_{a2}$ has a tiny effect on $\theta_{a6}$.

Fig.6 demonstrates the positions of transmission poles with varied electrical lengths for each stub. In Fig.6, when $\theta_{a2}$ enlarges to 27° and $\theta_{a5}$ declines to 11° are simulated for the first pole $f_{a1Left}$ which shifts to a lower frequency. If $\theta_{a2}$ and $\theta_{a5}$ are used to independently tune $f_{a2Right}$ and $f_{a3Left}$, respectively, as can be seen, the second pole $f_{a2Right}$ to a higher frequency while the third $f_{a3Left}$ will shift to a lower frequency. It can be found that each transmission pole can be independently managed in a wide frequency range.

The coupling routing scheme of Tri-band BPF is given in Fig.7. For proposing more choices in designing the bandwidths for three passbands simultaneously, four design freedoms are chosen as coupling spacing $S_{a1}/S_{a2}$ and the coupling length $L_{a1}/L_{a7}$. The actual coupling coefficients between the modes can be computed from the following (26).

$$K = \frac{f_H^2 - f_L^2}{f_H^2 + f_L^2} \tag{26}$$

where $f_H$ and $f_L$ are the higher and lower cutoff frequencies of each passband. The corresponding coupling coefficients versus the varied value of $S_{a1}$ and the length of coupled lines $L_{a1}$ of coupled Tri-band BPF are sketched in Fig.8. The coupling coefficients $K_{Tri1}$, $K_{Tri2}$, and $K_{Tri3}$ for each passband are illustrated in Fig.8(a), respectively. For the fixed $L_{a1}$, all the coupling coefficients decrease as $S_{a1}$ enlarges. Meanwhile, the coupling coefficients are raised as $L_{a1}$ increases when $S_{a1}$ keeps remains unchanged. Moreover, it can be observed that $S_{a1}$ mainly influence $K_{Tri1}$ and $K_{Tri2}$. While a slight increase in $K_{Tri1}$, $K_{Tri2}$, and $K_{Tri3}$ with an increase in the length of coupled lines $L_{a1}$. Subsequently, the Fig.9

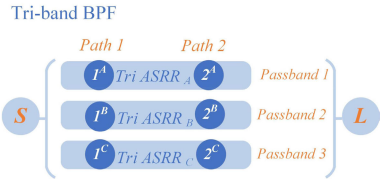


**FIGURE 7.** Dual-path coupling architecture for Tri-band transversal filter design.

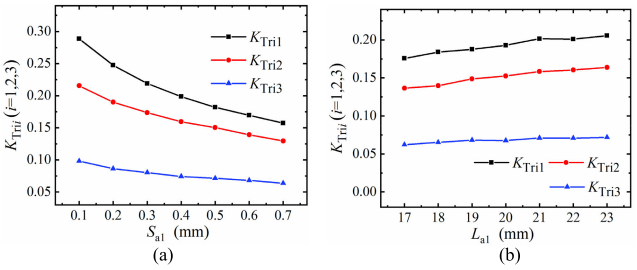


**FIGURE 8.** Coupling coefficient of $K_{Tri}$ for triple-passband versus different (a) $S_{a1}$ (b) $L_{a1}$.

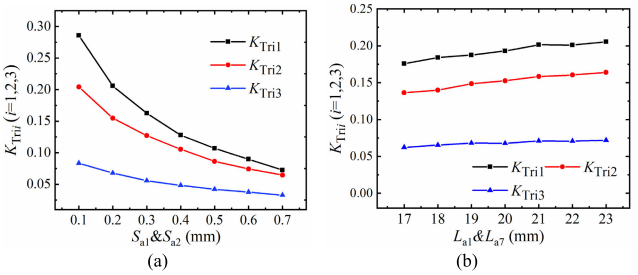


**FIGURE 9.** Coupling coefficient of $K_{Tri}$ for triple-passband versus different (a) $S_{a1}$ & $S_{a2}$ (b) $L_{a1}$ & $L_{a7}$.

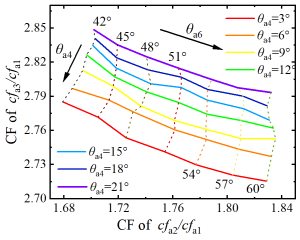


**FIGURE 10.** Design graph of $cf_{a3}/cf_{a1}$ and $cf_{a2}/cf_{a1}$ versus varied $\theta_{a4}$ and $\theta_{a6}$.

is achieved by manipulating two coupling spacings $S_{a1}$&$S_{a2}$ or coupling lengths $L_{a1}$&$L_{a7}$. Meanwhile, owing to the different coupling length or coupling spacing between two parallel coupling lines, the external coupling generates more changes.

Extraction method of the center frequency(CF):

$$CF = f_H - f_L \tag{27}$$

where $f_H$ and $f_L$ are the higher and lower cutoff frequencies of each passband. Fig.10 illustrates centre frequencies versus varied $\theta_{a4}$ and $\theta_{a6}$. It can be seen that $cf_{a3}/cf_{a1}$ and $cf_{a2}/cf_{a1}$

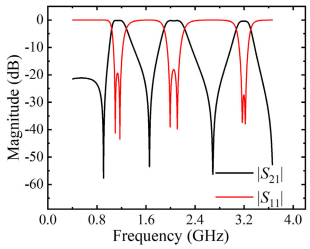


**FIGURE 11.** Simulated predicted frequency responses of proposed Tri-band BPF.

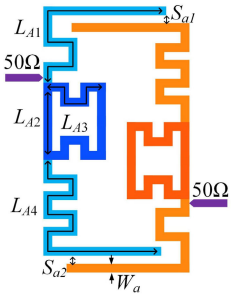


**FIGURE 12.** Geometrical schematic of presented Tri-band BPF.

both increase as an increase $\theta_{a4}$ from 3° to 21° when $\theta_{a6}$ is fixed at a certain value. Similarly, the tendencies ratio of the $cf_{a2}/cf_{a1}$ variation enlarged when $\theta_{a6}$ increases, while $cf_{a3}/cf_{a1}$ is opposed. This reveals that triple frequency bands constructed by Tri-band BPF can be independently controlled.

As demonstrated in Fig.11, the S-parameter responses of the wideband BPF are simulated using the ideal Tri-band BPF. The geometrical schematic corresponding to Fig.1(b) has been listed in Fig.12.

## III. QUAD-BAND AND QUINT-BAND BPF ANALYSIS AND DESIGN

By adding the extra open-ended stub, the Quad-ASRR and the Quint-ASRR are constructed based on the Tri-ASRR, where the Quad-ASRR and Quint-ASRR can be employed to exploit a quad-band BPF and quint-band BPF. The resonator structure of Quad-ASRR and Quint-ASRR are shown in Fig.13. The corresponding physical lengths and widths are represented by $L_{B1}$ to $L_{B6}$, $W_b$, $L_{C1}$ to $L_{C8}$ and $W_c$, respectively. To further demonstrate the characteristics of the proposed resonator, Fig.14 depicts the ideal transmission line model (TLM) of Quad-ASRR and Quint-ASRR. As shown in Fig.14(a), $Y_{Bn}$ ($n = 1, 2, 3, 4, 5$ and 6) and $\theta_{Bn}$ ($n = 1, 2, 3, 4, 5$ and 6) describe the characteristic admittances and electrical lengths of the counterpart microstrip line. And $Y_{Cn}$ ($n = 1, 2, 3, 4, 5, 6, 7$ and 8) and $\theta_{Cn}$ ($n = 1, 2, 3, 4, 5, 6, 7$ and 8) represent the characteristic admittances and electrical lengths of the Quint-ASRR, respectively.

The electrical parameters of Quad-ASRR and Quint-ASRR are portrayed in Fig.15. Herein, $Y_{inb}$ and $Y_{inc}$ are input admittances of ASRRs with electrical parameters identical to Fig.14. Furthermore, the design methodology is investigated

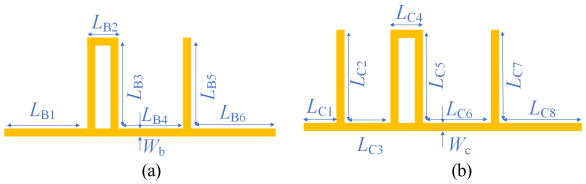


**FIGURE 13.** Basic structure (a) Quad-ASRR (b) Quint-ASRR.

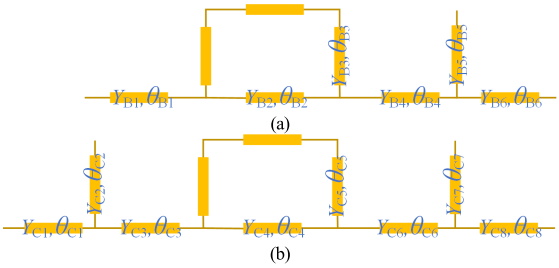


**FIGURE 14.** Transmission line model of (a) Quad-ASRR (b) Quint-ASRR.

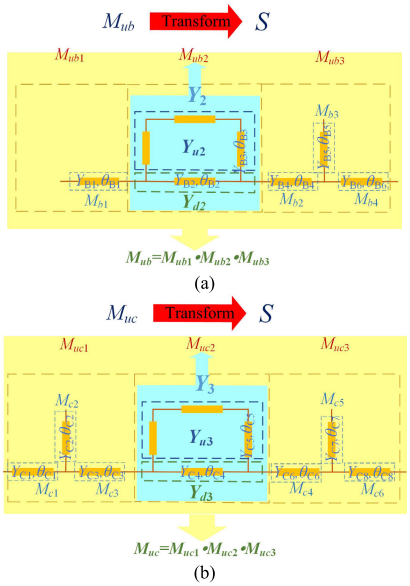


**FIGURE 15.** Equivalent ideal transmission line model for diagram analysis (a) Quad-ASRR (b) Quint-ASRR.

by accompany adopt the ABCD matrix, $Y$ matrix accompany with $S$ matrix which is similar to Tri-ASRR. The $Y_{inc}$ of Quint-ASRR will be elaborated in the following sections. For simplicity, $Y_{C1} = Y_{C2} = Y_{C3} = Y_{C4} = Y_{C5} = Y_{C6} = Y_{C7} = Y_{C8}$ is assumed. Since the ABCD matrix of microstrip line can be respectively defined as:

$$M_{c1} = \begin{bmatrix} \cos\theta_{C1} & j\frac{1}{Y_{C1}}\sin\theta_{C1} \\ jY_{C1}\sin\theta_{C1} & \cos\theta_{C1} \end{bmatrix} \tag{28}$$

$$M_{c2} = \begin{bmatrix} 1 & 0 \\ jY_{C1}\tan\theta_{C2} & 1 \end{bmatrix} \tag{29}$$

$$M_{c3} = \begin{bmatrix} \cos\theta_{C3} & j\frac{1}{Y_{C1}}\sin\theta_{C3} \\ jY_{C1}\sin\theta_{C3} & \cos\theta_{C3} \end{bmatrix} \tag{30}$$

$$M_{uc1} = M_{c1} \cdot M_{c2} \cdot M_{c3} = \begin{bmatrix} A & B \\ C & \mathrm{D} \end{bmatrix}_{uc1} \tag{31}$$

where:

$$\begin{aligned} A_{uc1} &= \cos\theta_{C1}\cos\theta_{C1} - \sin\theta_{C1}\tan\theta_{C2}\cos\theta_{C3} \\ &\quad - \sin\theta_{C1}\sin\theta_{C3} \end{aligned} \tag{32}$$

$$\begin{aligned} B_{uc1} &= j\frac{1}{Y_{C1}}\cos\theta_{C1}\sin\theta_{C3} - j\frac{1}{Y_{C1}}\cos\theta_{C1}\tan\theta_{C2}\sin\theta_{C3} \\ &\quad + j\frac{1}{Y_{C1}}\sin\theta_{C1}\cos\theta_{C3} \end{aligned} \tag{33}$$

$$\begin{aligned} C_{uc1} &= jY_{C1}\sin\theta_{C1}\cos\theta_{C3} + jY_{C1}\cos\theta_{C1}\tan\theta_{C2}\sin\theta_{C3} \\ &\quad + jY_{C1}\cos\theta_{C1}\sin\theta_{C3} \end{aligned} \tag{34}$$

$$\begin{aligned} D_{uc1} &= -\sin\theta_{C1}\sin\theta_{C3} - \cos\theta_{C1}\tan\theta_{C2}\sin\theta_{C3} \\ &\quad + \cos\theta_{C1}\cos\theta_{C3} \end{aligned} \tag{35}$$

Similarly, the Muc3 has:

$$M_{uc3} = M_{c4} \cdot M_{c5} \cdot M_{c6} = \begin{bmatrix} A & B \\ C & \mathrm{D} \end{bmatrix}_{uc3} \tag{36}$$

$$\begin{aligned} A_{uc3} &= \cos\theta_{C6}\cos\theta_{C6} - \sin\theta_{C6}\tan\theta_{C7}\cos\theta_{C8} \\ &\quad - \sin\theta_{C6}\sin\theta_{C8} \end{aligned} \tag{37}$$

$$\begin{aligned} B_{uc3} &= j\frac{1}{Y_{C6}}\cos\theta_{C6}\sin\theta_{C6} - j\frac{1}{Y_{C6}}\cos\theta_{C6}\tan\theta_{C7}\sin\theta_{C8} \\ &\quad + j\frac{1}{Y_{C6}}\sin\theta_{C6}\cos\theta_{C8} \end{aligned} \tag{38}$$

$$\begin{aligned} C_{uc3} &= jY_{C6}\sin\theta_{C6}\cos\theta_{C6} + jY_{C6}\cos\theta_{C6}\tan\theta_{C7}\sin\theta_{C8} \\ &\quad + jY_{C6}\cos\theta_{C6}\sin\theta_{C8} \end{aligned} \tag{39}$$

$$\begin{aligned} D_{uc3} &= -\sin\theta_{C6}\sin\theta_{C8} - \cos\theta_{C6}\tan\theta_{C7}\sin\theta_{C8} \\ &\quad + \cos\theta_{C6}\cos\theta_{C8} \end{aligned} \tag{40}$$

The second part of the circuit is divided into the road and lower road, which belongs to the parallel network, using the Y matrix calculation from the definition:

$$M_{uc2} = [Y_3] = [Y_{u3}] + [Y_{d3}] \tag{41}$$

For transmission Mua2, the Y matrix can be obtained as follows:

$$\begin{aligned} &\begin{bmatrix} Y_{11} & Y_{12} \\ Y_{21} & Y_{22} \end{bmatrix} \\ &= \begin{bmatrix} \frac{D}{B} & \frac{-(AD-BC)}{B} \\ \frac{-1}{B} & \frac{A}{B} \end{bmatrix} \end{aligned} \tag{42}$$

$$[Y_{11}]_{u3} = \frac{Y_{C4}\cos(\theta_{C4}+2\theta_{C5})}{j\sin(\theta_{C4}+2\theta_{C5})} \tag{43}$$

$$[Y_{12}]_{u3} = \frac{-Y_{C4}(\cos^2(\theta_{C4}+2\theta_{C5}) + \sin^2(\theta_{C4}+2\theta_{C5}))}{j\sin(\theta_{C4}+2\theta_{C5})} \tag{44}$$

$$[Y_{21}]_{u3} = \frac{-Y_{C4}}{j\sin(\theta_{C4}+2\theta_{C5})} \tag{45}$$

$$[Y_{22}]_{u3} = \frac{Y_{C4}\cos\theta_{C5}}{j\sin(\theta_{C4}+2\theta_{C5})} \tag{46}$$

$$\begin{aligned} &\begin{bmatrix} Y_{11} & Y_{12} \\ Y_{21} & Y_{22} \end{bmatrix}_{d3} \\ &= \begin{bmatrix} \frac{Y_{C4}\cos\theta_{C4}}{j\sin\theta_{C4}} & \frac{-Y_{C4}(\cos^2\theta_{C5}+\sin^2\theta_{C5})}{j\sin\theta_{C5}} \\ \frac{-Y_{C4}}{j\sin\theta_{C5}} & \frac{Y_{C4}\cos\theta_{C5}}{j\sin\theta_{C5}} \end{bmatrix} \end{aligned} \tag{47}$$

$$[Y_{11}]_3 = \frac{Y_{C4}\cos(\theta_{C4}+2\theta_{C5})}{j\sin(\theta_{C4}+2\theta_{C5})} + \frac{Y_{C4}\cos Y_{C4}}{j\sin\theta_{C4}} \tag{48}$$

$$\begin{aligned} [Y_{12}]_3 &= \frac{-Y_{C4}(\cos^2(\theta_{C4}+2\theta_{C5}) + \sin^2(\theta_{C4}+2\theta_{C5}))}{j\sin(\theta_{C4}+2\theta_{C5})} \\ &\quad + \frac{-Y_{C4}(\cos^2\theta_{C4} + \sin^2\theta_{C4})}{j\sin\theta_{C4}} \end{aligned} \tag{49}$$

$$[Y_{21}]_3 = \frac{-Y_{C4}}{j\sin(\theta_{C4}+2\theta_{C5})} + \frac{-Y_{C4}}{j\sin\theta_{C4}} \tag{50}$$

$$[Y_{22}]_3 = \frac{Y_{C4}\cos(\theta_{C4}+2\theta_{C5})}{j\sin(\theta_{C4}+2\theta_{C5})} + \frac{Y_{C4}\cos\theta_{C4}}{j\sin\theta_{C4}} \tag{51}$$

Convert Y matrix into the ABCD matrix is:

$$\begin{aligned} M_{uc3} &= \begin{bmatrix} A & B \\ C & D \end{bmatrix}_{c1} \\ &= \begin{bmatrix} \frac{-Y_{11}}{Y_{21}} & \frac{-1}{Y_{21}} \\ \frac{-(Y_{11}Y_{22}-Y_{12}Y_{21})}{Y_{21}} & \frac{-Y_{11}}{Y_{21}} \end{bmatrix} \\ &= \frac{1}{Y_{21}}\begin{bmatrix} -Y_{22} & -1 \\ -(Y_{11}-Y_{22}) & -Y_{11} \end{bmatrix} \end{aligned} \tag{52}$$

$$\begin{aligned} [A]_{uc3} &= \frac{\sin(\theta_{C4}+2\theta_{C5})\sin\theta_{C4}}{\sin(\theta_{C4}+2\theta_{C5}) + \sin\theta_{C4}} \\ &\quad \times \left(\frac{\cos(\theta_{C4}+2\theta_{C5})}{\sin(\theta_{C4}+2\theta_{C5})} + \frac{\cos\theta_{C4}}{\sin\theta_{C4}}\right) \end{aligned} \tag{53}$$

$$[B]_{uc3} = \frac{\sin(\theta_{C4}+2\theta_{C5})\sin\theta_{C4}}{\sin(\theta_{C4}+2\theta_{C5}) + \sin\theta_{C4}} \tag{54}$$

$$\begin{aligned} [C]_{uc3} &= \frac{\sin(\theta_{C4}+2\theta_{C5})\sin\theta_{C4}}{\sin(\theta_{C4}+2\theta_{C5}) + \sin\theta_{C4}} \\ &\quad \times \frac{Y_{C4}}{j}\left(\left(\frac{\cos(\theta_{C4}+2\theta_{C5})}{\sin(\theta_{C4}+2\theta_{C5})} + \frac{\cos\theta_{C4}}{\sin\theta_{C4}}\right)^2\right. \\ &\quad \left. - \left(\frac{-1}{\sin(\theta_{C4}+2\theta_{C5})} + \frac{-1}{\sin\theta_{C4}}\right)^2\right) \end{aligned} \tag{55}$$

$$\begin{aligned} [D]_{uc3} &= \frac{\sin(\theta_{C4}+2\theta_{C5})\sin\theta_{C4}}{\sin(\theta_{C4}+2\theta_{C5}) + \sin\theta_{C4}} \\ &\quad \times \left(\frac{\cos(\theta_{C4}+2\theta_{C5})}{\sin(\theta_{C4}+2\theta_{C5})} + \frac{\cos\theta_{C4}}{\sin\theta_{C4}}\right) \end{aligned} \tag{56}$$

The ABCD matrix of the Quint-ASRR BPFs is:

$$M_{uc} = \begin{bmatrix} A & B \\ C & D \end{bmatrix}_3 = M_{uc1} \cdot M_{uc2} \cdot M_{uc3} \tag{57}$$

Similarly, the overall ABCD matrix of the Quad-ASRR can be obtained:

$$M_{ub} = \begin{bmatrix} A & B \\ C & D \end{bmatrix}_2 = M_{ub1} \cdot M_{ub2} \cdot M_{ub3} \tag{58}$$

The conversion relationship between the ABCD matrix and the S parameter matrix is:

$$\begin{bmatrix} S_{11} & S_{12} \\ S_{21} & S_{21} \end{bmatrix} = \begin{bmatrix} \frac{A+BY_0-C/Y_0-D}{A+BY_0+C/Y_0+D} & \frac{2(AD-BC)}{A+BY_0+C/Y_0+D} \\ \frac{2}{A+BY_0+C/Y_0+D} & \frac{-A+BY_0-C/Y_0+D}{A+BY_0+C/Y_0+D} \end{bmatrix} \tag{59}$$

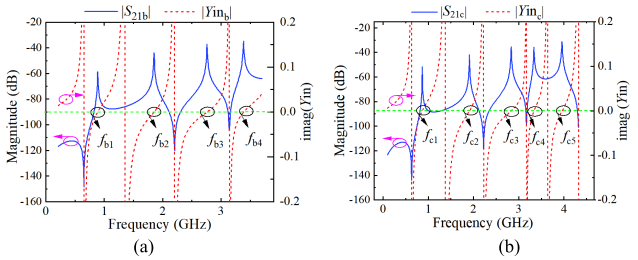


**FIGURE 16.** The Imaginary part of input admittance $Y_{in}$ of (a) Quad-ASRR (b) Quint-ASRR.

where $Y_C = Y_{C1} = Y_{C2} = Y_{C4} = Y_{C5} = Y_{C6} = Y_{C7} = Y_{C8}$ is the characteristic impedance of the microstrip line. For simplicity, $\theta_{C2} = \theta_{C3} = \theta_{C4} = \theta_{C7} = 30°$, $\theta_{C1} = \theta_{C2} = \theta_{C8} = 2\theta_{C2} = 60°$, $\theta_{C5} = 4\theta_{C2} = 120°$ are assumed. For Quint-ASRR, $Y_{B1} = Y_{B2} = Y_{B3} = Y_{B4} = Y_{B5} = Y_{B6}$ is the characteristic impedance of the microstrip line. For simplicity, $\theta_{B2} = \theta_{B3} = 30°$, $\theta_{B6} = 2\theta_{B2} = 60°$, $\theta_{B1} = \theta_{B4} = 4\theta_{B2} = 120°$. In order to find the input admittance, as defined by the ABCD matrix:

$$\begin{bmatrix} V_1 \\ I_1 \end{bmatrix} = \begin{bmatrix} A & B \\ C & D \end{bmatrix} \begin{bmatrix} V_2 \\ I_2 \end{bmatrix} \Rightarrow \begin{cases} V_{c1} = AV_{c2} + BI_{c2} \\ I_{c1} = CV_{c2} + DI_{c2} \end{cases} \tag{60}$$

According to the above definition formula, the input admittance $Y_{in}$ is calculated by the resonator ABCD:

$$Y_{inc} = \frac{I_{c1}}{V_{c1}} = \frac{CV_{c2} + DI_{c2}}{AV_{c2} + BI_{c2}} = \frac{CZ_{cL} + D}{AZ_{cL} + B} \tag{61}$$

thus:

$$Z_c = V_{c2}/I_{c2} \tag{62}$$

$$Y_{inc} = \frac{C}{A} \tag{63}$$

According to resonant condition $\mathrm{Im}(Y_{\mathrm{in}}) = 0$, the imaginary part of the input admittance in Quad-ASRR and Quint-ASRR plotted in Fig.16. It can be observed from Fig.16(a) that Quad-ASRR yields quadruple transmission poles $f_{b1}, f_{b2}, f_{b3}$ and $f_{b4}$. Similarly, Quint-ASRR yields quintuple transmission poles $f_{c1}, f_{c2}, f_{c3}, f_{c4}$ and $f_{c5}$ are depicted in Fig.16(b). Among them, $f_{c1}$ forms a group that falls within the range of the first desired frequency band, while $f_{c2}, f_{c3}, f_{c4}$ and $f_{c5}$ fall within the design range of the second, third, fourth and fifth frequency bands, respectively. And the transmission poles of Quad-ASRR and Quint-ASRR can be employed for the construction of the different frequency bands.

The ideal transmission line model of Quad-BPF and Quint-BPF are sketched in Fig.17(a), where the parameters $Y_{bn}$ and $\theta_{bn}$ ($n$ = 1,2,3,4,5,6,7,8) represent the characteristic admittances and electrical lengths of the Quad-band BPF, respectively. It can be observed from Fig.17(b), the detailed electrical parameters are separately $Y_{cn}$ and $\theta_{cn}$ ($n$ = 1,2,3,4,5,6,7,8,9).

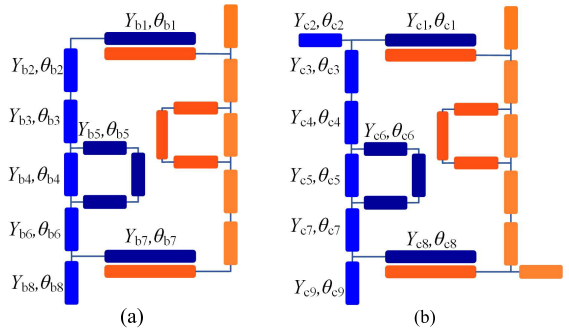


**FIGURE 17.** (a) Equivalent ideal transmission line model of proposed Quad-band BPF. (b) Equivalent ideal transmission line model of proposed Quint-band BPF.

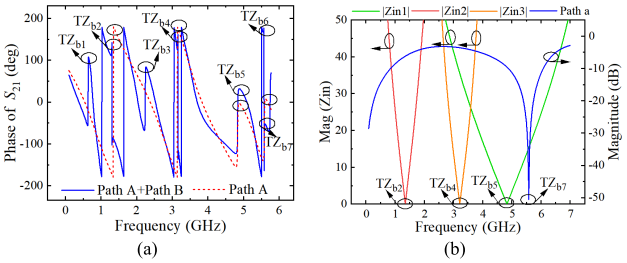


**FIGURE 18.** (a) Quad-band BPF phase shift of $S_{21}$ Path A and Path B. (b) Simulated transmission coefficient corresponding TZs of Zin1, Zin2, Zin3 and Path a.

The phase shift of $S_{21}$ of Path A and Path A+Path B are respectively illustrated in Fig.18(a). As can be observed from Fig.18(a) there are four transmission zeros ($TZ_{b2}$, $TZ_{b4}$, $TZ_{b5}$, $TZ_{b7}$) in Path A. However, by utilizing the transversal signal interaction techniques of the dual transmission path from the input port to the output port, seven transmission zeros ($TZ_{b1}$, $TZ_{b2}$, $TZ_{b3}$, $TZ_{b4}$, $TZ_{b5}$, $TZ_{b6}$, $TZ_{b7}$) can be yielded. Therefore, it reveals that the extra triple transmission zeros ($TZ_{b1}$, $TZ_{b3}$, $TZ_{b6}$) are formed by nested two identical ASRRs to achieve transversal signal interaction. As illustrated in Fig.18(b), the other four transmission zeros ($TZ_{b2}$, $TZ_{b4}$, $TZ_{b5}$, $TZ_{b7}$) are generated by different stubs. Similarly, the generation mechanism of transmission zeros ($TZ_{c1}$, $TZ_{c2}$, $TZ_{c3}$, $TZ_{c4}$, $TZ_{c5}$, $TZ_{c6}$, $TZ_{c7}$, $TZ_{c8}$, $TZ_{c9}$, $TZ_{c10}$) of Quint-BPF are shown in Fig.19. The TZs versus various $L_{b3}$ and $L_{c3}$ values are shown in Fig.20(a) and Fig.20(b). It can be seen in Fig.20(a) that $TZ_{b1}$, $TZ_{b2}$, $TZ_{b3}$, $TZ_{b4}$, $TZ_{b5}$ and $TZ_{b6}$ remain almost unchanged as $L_{b3}$ varies, while the variation of $L_{b3}$ has an obvious effect on $TZ_{b7}$. As depicted in Fig.20(b), it can be seen that $TZ_{c6}$, $TZ_{c9}$ and $TZ_{c10}$ decreases as $L_{c3}$ enlarged, while other transmission zeros ($TZ_{c1}$, $TZ_{c2}$, $TZ_{c3}$, $TZ_{c4}$, $TZ_{c5}$, $TZ_{c7}$, $TZ_{c8}$) is almost unchanged. In Fig.20, the 1st, 2nd, 3rd,4th and 5th respectively denote the first, second, third, fourth and fifth range of each passband.

Fig.21 demonstrates the positions of transmission poles of Quad-ASRR and Quint-ASRR with varied electrical lengths for each stub. In Fig.21(a), when $\theta_{b2} = 10°$ and $\theta_{b5} = 29°$ are simulated for the first pole $f_{b1\mathrm{Right}}$ which shifts to

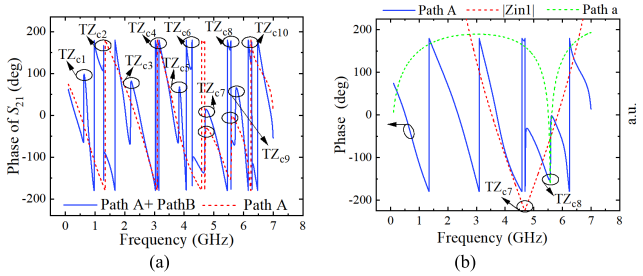


**FIGURE 19.** (a) Quint-band BPF phase shift of $S_{21}$ Path A and Path B. (b) Simulated transmission coefficient corresponding TZs of Zin1 and Path a.

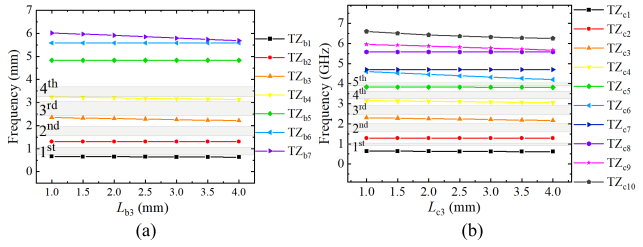


**FIGURE 20.** (a) Quad-band TZs versus $L_{b3}$. (b) Quint-band TZs versus varied $L_{c3}$.

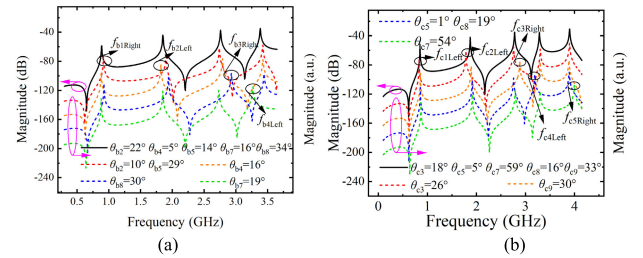


**FIGURE 21.** Transmission coefficient of quadruple/quintuple varied conditions under weak coupling. (a) Quad-ASRR. (b) Quint-ASRR.

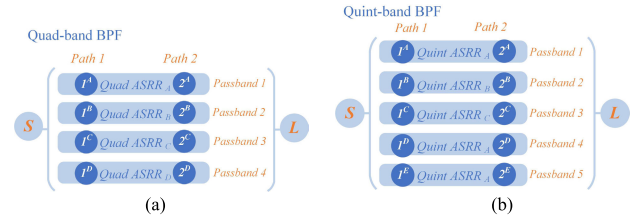


**FIGURE 22.** (a) Dual-path coupling architecture for Quad-band BPF transversal filter design. (b) Dual-path coupling architecture for Quint-band BPF transversal filter design.

a higher frequency. Meanwhile, $f_{b2Left}$ and $f_{b4Left}$ shift to a lower frequency, $f_{b3Right}$ shift to a higher frequency, when $\theta_{b8}$, $\theta_{b4}$, and $\theta_{b7}$ are respectively selected as 30°, 16° and 19° respectively. In Fig.21(b), when $\theta_{c3} = 26°$ is predicted for the poles $f_{c1Left}$ and $f_{c2Left}$ which shift to a lower frequency. Similarly, the third and fifth passband will shift to a higher frequency with increased $\theta_{c9}$ and $\theta_{c7}$, respectively. And when $\theta_{c5} = 1°$ and $\theta_{c8} = 29°$ are chosen, the third pole $f_{c3Right}$ shifts to a higher frequency.

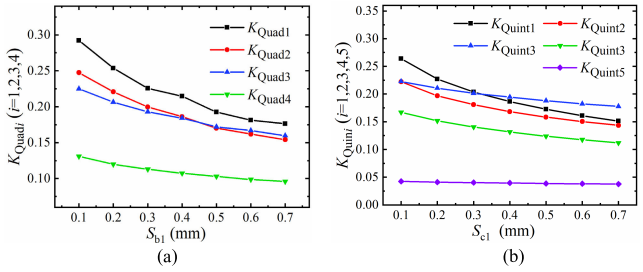


**FIGURE 23.** Coupling coefficient of $K_{Quad}/K_{Quint}$ for quadruple/quintuple-passband versus different (a)$S_{b1}$ (b) $S_{c1}$.

The coupling coefficient is an integral part of the design of BPFs, and this feature is discussed in detail in Fig.22 to Fig.26. Fig.22 illustrates the specific coupling schemes utilized in Quad-band and Quint-band BPF. The Quad-band and Quint-band BPF are coupled by two asymmetric stubs, Path1 and Path2, respectively. Quad-band BPFs generates four bands, namely Passband1, Passband2, Passband3, and Passband4, while Quint-band BPFs generates five bands, namely Passband1, Passband2, Passband3, Passband4, and Passband5. In order to propose a more optimal frequency BPF design, this section presents the bands of Quad-band BPF and Quint-band BPF in Fig.23 to Fig.26. This is achieved by manipulating the coupling spacing $S_{b1}/S_{b2}/S_{c1}/S_{c2}$ and the coupling length $L_{b1}/L_{b7}/L_{c1}/L_{c7}$ which represents degrees of freedom in the design. The extraction method of the coupling coefficient is established as follows:

$$K = \frac{f_H^2 - f_L^2}{f_H^2 + f_L^2} \tag{64}$$

where $f_H$ and $f_L$ are the higher and lower cutoff frequencies of each passband. The coupling routing scheme of Quad-BPFs and Quint-BPFs are given in Fig.22. To provide more choices in designing the bandwidths for four and five passbands simultaneously, the coupling spacings($S_{b1}/S_{b2}/S_{c1}/S_{c2}$) and the coupling lengths($L_{b1}/L_{b7}/L_{c1}/L_{c7}$) are applied to design the Quad-BPFs and Quint-BPFs coupling structure. The actual coupling coefficients between the modes can be computed from the following (63). It can be observed from Fig.23 and Fig.24 that the coupling coefficients of Quad-BPFs($K_{Quad1}$, $K_{Quad2}$, $K_{Quad3}$, $K_{Quad4}$) and the coupling coefficients of Quint-BPFs( $K_{Quint1}$, $K_{Quint2}$, $K_{Quint3}$, $K_{Quint4}$, $K_{Quint5}$) will be decreased as the coupled spacing($S_{b1}$, $S_{c1}$) increases or the coupled length ($L_{b1}$, $L_{c1}$) narrows down. Moreover, the Fig.25 and Fig.26 are achieved by manipulating two coupling spacings ($S_{b1}\&S_{b2}/S_{c1}\&S_{c2}$) or coupling lengths( $L_{b1}\&L_{b7}/L_{c1}\&L_{c7}$).

Fig.27 illustrates the centre frequencies of Quad-BPF versus varied $\theta_{b2}$ and $\theta_{b4}$. It can be observed that $cf_{b3}/cf_{b1}$ and $cf_{b2}/cf_{b1}$ both decrease as increases $\theta_{b2}$ from 22° to 28°, while $cf_{b4}/cf_{b1}$ has an opposed trend. Similarly, when $\theta_{a6}$ is fixed at a certain value, the tendencies ratio of $cf_{b3}/cf_{b1}$ and $cf_{b4}/cf_{b1}$ variation enlarged when $\theta_{b6}$ increases, while $cf_{b2}/cf_{b1}$ decreases. The centre frequencies of Quint-BPF

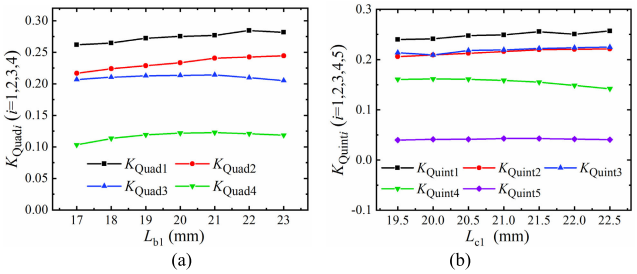


**FIGURE 24.** Coupling coefficient of $K_{Quad}/K_{Quint}$ for quadruple/quintuple-passband versus different (a)$L_{b1}$ (b) $L_{c1}$.

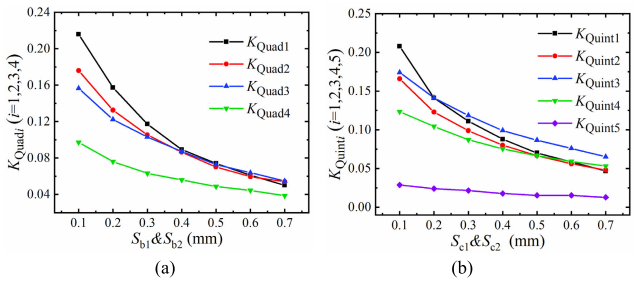


**FIGURE 25.** Coupling coefficient of $K_{Quad}/K_{Quint}$ for quadruple/quintuple-passband versus different (a)$S_{b1}$ & $S_{b2}$ (b) $Sy_{c1}$ & $S_{c2}$.

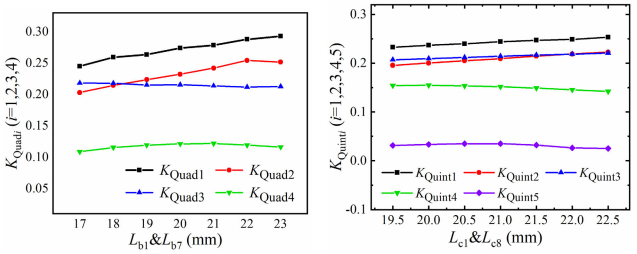


**FIGURE 26.** Coupling coefficient of $K_{Quad}/K_{Quint}$ for quadruple/quintuple-passband versus different (a)$L_{b1}$ & $L_{b7}$ (b) $L_{c1}$ & $L_{c8}$.

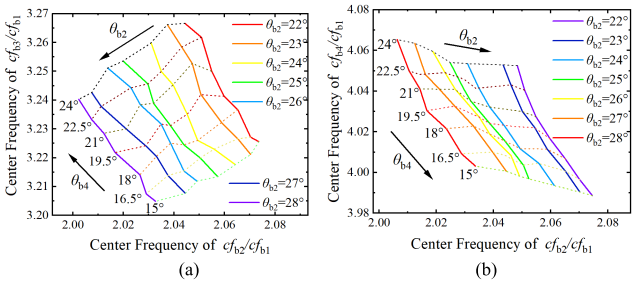


**FIGURE 27.** (a) Design graph of $cf_{b3}/cf_{b1}$ and $cf_{b2}/cf_{b1}$ versus varied $\theta_{b2}$ and $\theta_{b4}$. (b) Design graph of $cf_{b4}/cf_{b1}$ and $cf_{b2}/cf_{b1}$ versus varied $\theta_{b2}$ and $\theta_{b4}$.

versus varied $\theta_{c3}$ and $\theta_{c7}$ are plotted in Fig.28. It can be seen that $cf_{c3}/cf_{c1}$ and $cf_{c4}/cf_{c1}$ both increase as increases $\theta_{c3}$ from 17° to 23° when $\theta_{a6}$ is fixed at a certain value. Meanwhile, $cf_{c2}/cf_{c1}$ and $cf_{c5}/cf_{c1}$ are both decreased. As shown in the Fig.28, the larger $\theta_{c7}$ is, the larger $cf_{c3}/cf_{c1}$,$cf_{c4}/cf_{c1}$ and

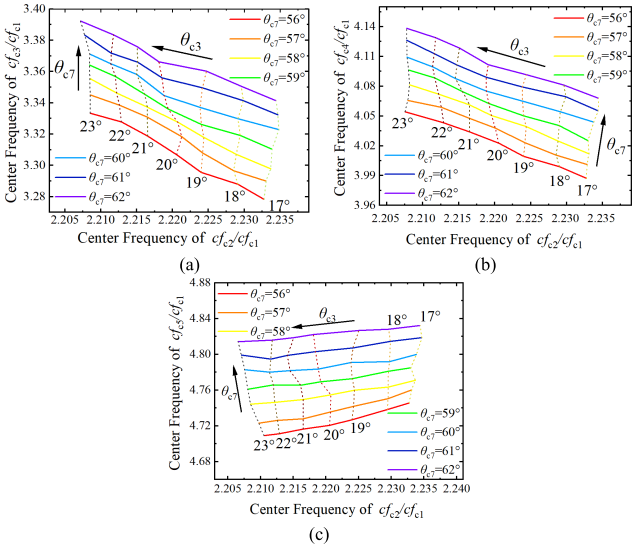


**FIGURE 28.** (a) Design graph of $cf_{c3}/cf_{c1}$ and $cf_{c2}/cf_{c1}$ versus varied $\theta_{c3}$ and $\theta_{c7}$. (b) Design graph of $cf_{c4}/cf_{c1}$ and $cf_{c2}/cf_{c1}$ versus varied $\theta_{c3}$ and $\theta_{c7}$. (c) Design graph of $cf_{c5}/cf_{c1}$ and $cf_{c2}/cf_{c1}$ versus varied $\theta_{c3}$ and $\theta_{c7}$.

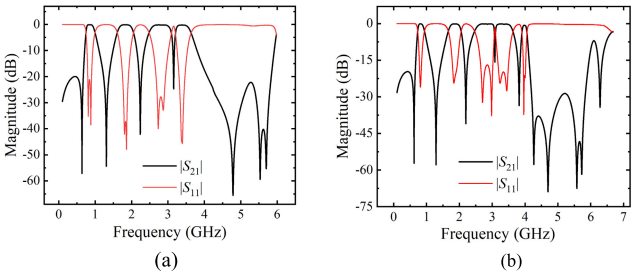


**FIGURE 29.** Simulated predicted frequency responses of proposed Quad-band BPF. (b) Quint-band BPF.

$cf_{c5}/cf_{c1}$ are, while $\theta_{c7}$ has a minor effect on $cf_{c2}/cf_{c1}$. The center frequency(CF) of each passband can be defined as below:

$$CF = f_H - f_L \tag{65}$$

where $f_H$ and $f_L$ are the higher and lower cutoff frequency of each passband.

As demonstrated in Fig.29, the $S$-parameter responses of the wideband BPF are characteristics by utilizing the transmission line model of Quad-bans BPF and Quint-band BPF. The geometrical dimensions corresponding to transmission line model of Fig.13 have been illustrated in Fig.27.

Fig.31 shows the simulated current density distribution of the designed BPFs at center frequencies. It can be observed that the current is mainly concentrated on the $Y_{a6}$ and its symmetric segment of the Tri-band BPF at the first CF. Furthermore, at the second CF of Tri-band BPF, the current is mainly concentrated on the $Y_{a2}$ to $Y_{a3}$ and its symmetric segment. And for the third CF, the current is mostly distributed on the $Y_{a6}$ to $Y_{a7}$ and its symmetric segment of the Tri-band BPF as depicted in Fig.31(a). Subsequently,

**TABLE 1. Comparison with similar references.**

| Ref. | CF (GHz) | Fbw (%) | IL(dB) | TZs | Independent Control of CFs | Each frequency band has a zero point | Extended |
|---|---|---|---|---|---|---|---|
| [1] | 2.7/3.67/5.44 | 20.1/14.7/26.3 | 1.2/2.3/1.6 | 5 | NO | YES | NO |
| [3] | 1.55/2.2/ 3.45/5.3 | / | 0.5/1/ 2.4/2.9 | 8 | NO | YES | NO |
| [6] | 2.4/3.5/ 5.2/5.8 | 6.7/7.2/ 6.9/5.3 | 2.0/1.9/ 1.9/1.96 | 8 | NO | NO | NO |
| [10] | 1.1/2.86 | 94/35.4 | / | 3 | NO | YES | NO |
| [14] | 3.7/6.6/9.0 | 7.52/5.1/4.44 | 0.99 / 1.17 / 1.5 | 3 | NO | NO | NO |
| [16] | 2.1/3.0/4.0/ 4.7/7.2 | 13.7/5.6/10.5/ 5.1/ 2.9 | 0.98/1.78/1.22/ 1.77/2.39 | 10 | NO | YES | NO |
| [17] | 1.8/3.3/4.5/ 5.5/6.2 | 3.3/9.8/3.4/ 3.2/2.1 | 2.6/0.8/1.9/ 2.5/2.9 | 2 | NO | NO | NO |
| [21] | 3.62/4.53/5.31 | 9.9/4.4/5.35 | 1.0/0.92/0.96 | 5 | YES | YES | NO |
| [23] | 2.48/3.45/ 5.17/5.78 | 5.96/6.43 / 5.96 /6.90 | 1.74/1.73/ 2.48/2.35 | 8 | YES | YES | NO |
| Tri-BPF | 1.15/2.05/3.18 | 13.6/12/4.4 | 0.92/0.93/1.58 | 4 | YES | YES | YES |
| Quad-BPF | 0.87/1.83/ 2.79/3.42 | 28.1/24/ 21.7/12.1 | 1.08/0.65/ 0.79/1.2 | 7 | YES | YES | YES |
| Quint-BPF | 0.83/1.86/2.77/ 3.37/3.98 | 24.3/20.7/21.5/ 15.4/3.5 | 0.73/0.71/0.18/ 0.34/1.67 | 10 | YES | YES | YES |

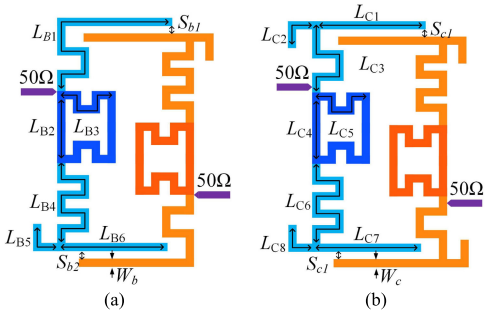


**FIGURE 30. Geometrical schematic of presented (a)Quad-band BPF (b)Quint-band BPF.**

the detailed current density distribution of the Quad-band BPF and Quint-band BPF are illustrated in Fig.31(b) and Fig.31(c).

## IV. SIMULATION AND TEST RESULTS OF THE CIRCUIT

The Tri-band BPF, Quad-band BPF and Quint-band BPF are simulated, fabricated, and evaluated to verify proposed theoretical design methodology. A photograph of the fabricated BPFs is shown in Fig.32. The proposed ASRRs are fabricated on the substrate of Rogers 4003C with a relative dielectric constant of 3.55, thickness of 0.508 mm, and loss tangent of 0.0027. By introducing a full wave electromagnetic (EM) simulator, the detailed physical dimensions of the ASRRs were optimized as follows, Tri band BPF: $L_{a1} = 5.1$, $L_{a2} = 6.4$, $L_{a3} = 1.5$, $L_{a4} = 2.6$, $L_{a5} = 18.5$, $L_{a6} = 24.5$, $L_{a7} = 21.3$; $W_{a1} = 0.7$; $S_{a1} = 0.35$, $S_{a2} = 0.35$ (units: mm). Quad-band BPF: $C_{b1} = 21.557$pf; $L_{b1} = 20.5$, $L_{b2} = 12.95$, $L_{b3} = 3.425$, $L_{b4} = 2.7$, $L_{b5} = 4$, $L_{b6} = 35.25$, $L_{b7} = 20.5$, $L_{b8} = 9.5$; $W_{b1} = 0.77$, $W_{b2} = 0.77$, $W_{b3} = 0.74$, $W_{b4} = 0.51$, $W_{b5} = 0.78$, $W_{b6} = 0.767$, $W_{b7} = 0.839$, $W_{b8} = 0.8$; $S_{b1} = 0.115$, $S_{b2} = 0.115$ (units: mm). Quint-band BPF: $C_{c1} = 43.014$pf; $L_{c1} = 20.5$, $L_{c2} = 8$, $L_{c3} = 6$, $L_{c4} = 3.425$, $L_{c5} = 3$, $L_{c6} = 7.9$, $L_{c7} = 36.05$, $L_{c8} = 20.5$, $L_{c9} = 9.8$; $W_{c1} = 0.68$, $W_{c2} = 0.767$, $W_{c3} = 0.68$, $W_{c4} = 0.61$, $W_{c5} = 0.6$, $W_{c6} = 0.075$, $W_{c7} = 0.71$, $W_{c8} = 0.969$, $W_{c9} = 0.9$; $S_{c1} = 0.135$, $S_{c2} = 0.135$ (units: mm).

The frequency responses of the presented BPFs is characteristics by using Anritsu MS4644 vector network analyzer. The measurement results are compared with simulation results in Fig.33, which exhibits ideal agreement between tested frequency responses and simulated frequency responses.

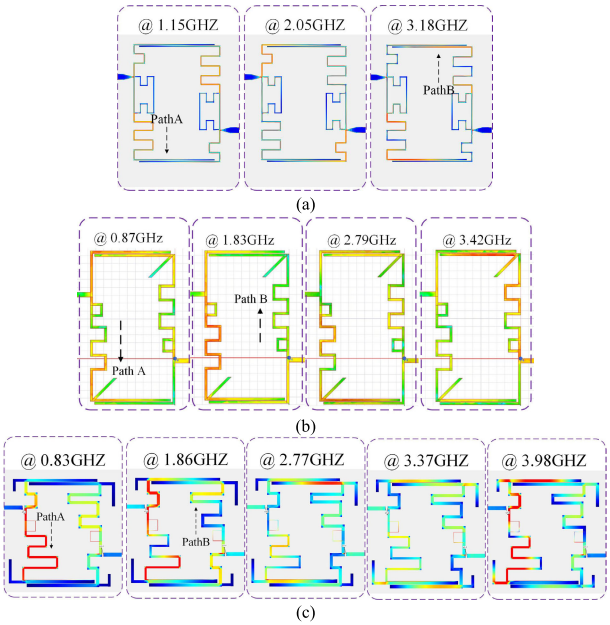


**FIGURE 31.** Current distribution at CF of operating frequencies. (a) Tri-band BPF (b)Quad-band BPF (c) Quint-band BPF.

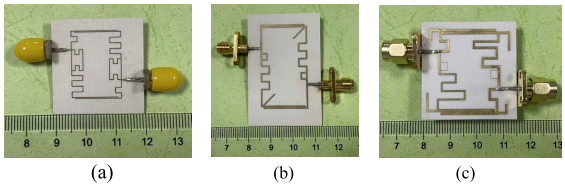


**FIGURE 32.** Photograph of fabricated prototype BPFs (a)Tri-band BPF (b)Quad-band BPF (c)Quint-band BPF.

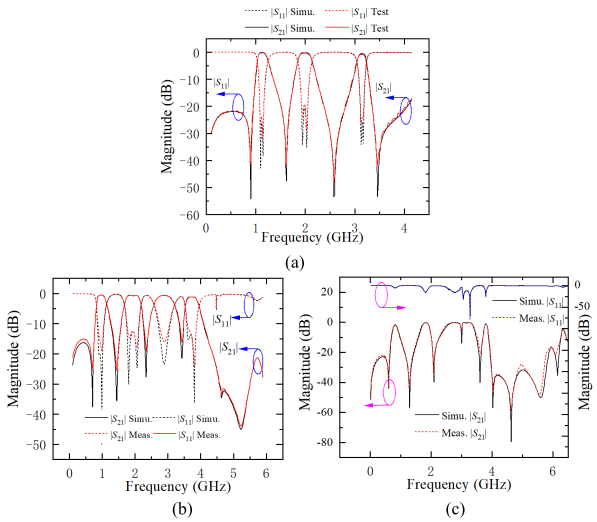


**FIGURE 33.** Comparison of measurement results between simulation predictions. (a)Tri-band BPF(b)Quad-band BPF (c)Quint-band BPF.

## V. CONCLUSION

Herein, we present the tri-/quad-/and quint band bandpass filter based on transversal signal interference concepts in this paper. The ABCD matrix Y matrix accompanied with *S* matrix were adopted to analyze design methodology. The filters are compact, independent and controllable frequency band characteristics, and abundant transmission zeros. The measurement results were in good agreement with the theoretical predictions. The proposed BPF can be easily proposed with expanded frequency band designs, which make the proposed filters attractive in multi-service wireless communication systems.

## ACKNOWLEDGMENT

The authors would like to express great appreciation to the editors and anonymous reviewers for their valuable comments and suggestions, which highly improved this paper. This work is supported by Natural Science Foundation of Tianjin (23YDTPJC00600) and Guangzhou Key Research & Development Program, Major Science and Technology Projects. (Grant No.202206070001).

## REFERENCES

[1] L. Gong, Y. Xiong, F. Zhang, L. Wang, Y. Sun, X. Zhao, M. He, L. Ji, X. Zhang, and B. Zhang, "A triple-wideband bandpass filter with controllable bandwidths based on stub-loaded resonators," *Int. J. Microw. Wireless Technol.*, vol. 10, no. 8, pp. 904–910, Oct. 2018.

[2] C. Zhu, J. Xu, W. Kang, and W. Wu, "High-selectivity tri-band bandpass filter with ultra-wide stopband," *Electron. Lett.*, vol. 51, no. 20, pp. 1585–1587, Oct. 2015.

[3] C. Cui and Y. Liu, "Quad-band bandpass filter design by embedding dual-band bandpass filter with dual-mode notch elements," *Electron. Lett.*, vol. 50, no. 23, pp. 1719–1720, Nov. 2014.

[4] F. Wei, B. Liu, Z. Li, L. Xu, R. Li, Y. Yang, and X.-N. Yang, "Balanced dual-band BPF and FPD using quad-mode RLR with improved selectivity," *IEEE Trans. Circuits Syst. II, Exp. Briefs*, vol. 69, no. 4, pp. 2081–2085, Apr. 2022.

[5] Z. J. Wang, C. Wang, and N. Y. Kim, "Dual-/triple-wideband microstrip bandpass filter using independent triple-mode stub-loaded resonator," *Microw. Opt. Technol. Lett.*, vol. 60, no. 1, pp. 56–64, Jan. 2018.

[6] T. Yan, X.-H. Tang, and J. Wang, "A novel quad-band bandpass filter using short stub loaded E-shaped resonators," *IEEE Microw. Wireless Compon. Lett.*, vol. 25, no. 8, pp. 508–510, Aug. 2015.

[7] W.-H. Tu and K.-W. Hsu, "Design of sext-band bandpass filter and sextaplexer using semilumped resonators for system in a package," *IEEE Trans. Compon., Packag., Manuf. Technol.*, vol. 5, no. 2, pp. 265–273, Feb. 2015.

[8] M. Tang, T. Shi, S. Chen, and H. Cao, "Dual-band bandpass filter based on a single triple-mode ring resonator," *Electron. Lett.*, vol. 52, no. 9, pp. 722–724, Apr. 2016.

[9] M. Xiao, X. Li, and G. Sun, "Quad-band bandpass filter based on single stepped-impedance ring resonator," *Electron. Lett.*, vol. 52, no. 10, pp. 848–849, May 2016.

[10] Q. Yang, Y.-C. Jiao, and Z. Zhang, "Compact multiband bandpass filter using low-pass filter combined with open stub-loaded shorted stub," *IEEE Trans. Microw. Theory Techn.*, vol. 66, no. 4, pp. 1926–1938, Apr. 2018.

[11] H. Liu, B. Ren, X. Guan, P. Wen, and Y. Wang, "Quad-band high-temperature superconducting bandpass filter using quadruple-mode square ring loaded resonator," *IEEE Trans. Microw. Theory Techn.*, vol. 62, no. 12, pp. 2931–2941, Dec. 2014.

[12] P. Wen, Z. Ma, S. Zhu, H. Liu, B. Ren, X. Guan, and M. Ohira, "Design of compact tri-band bandpass filter using stub-loaded quarter-wavelength SIRs," *IEICE Electron. Exp.*, vol. 16, no. 23, 2019, Art. no. 20190549.

[13] J. Xu, "Compact microstrip tri-band bandpass filter using new stubs loaded stepped-impedance resonator," *IEEE Microw. Wireless Compon. Lett.*, vol. 26, no. 4, pp. 249–251, Apr. 2016.

[14] A. Basit, M. I. Khattak, A. Althuwayb, and J. Nebhen, "Compact tri-band bandpass filter based on asymmetric step impedance resonators for Wimax and RFID systems," *J. Electromagn. Eng. Sci.*, vol. 21, no. 4, pp. 316–321, Sep. 2021.

[15] H. Liu, R. Wang, C. Lai, H. Li, and Z. Zuo, "A compact quint-band bandpass filter with high selectivity using uniform impedance resonators (UIRs)," in *IEEE MTT-S Int. Microw. Symp. Dig.*, Suzhou, China, Jul. 2020, pp. 1–3, doi: 10.1109/IMWS-AMP49156.2020.9199717.
[16] J. Ai, Y. Zhang, K. D. Xu, D. Li, and Y. Fan, "Miniaturized quint-band bandpass filter based on multi-mode resonator and $\lambda/4$ resonators with mixed electric and magnetic coupling," *IEEE Microw. Wireless Compon. Lett.*, vol. 26, no. 5, pp. 343–345, May 2016.
[17] W. Yang, L. Wang, L. Wang, and Y. Leng, "Design of a quint-band bandpass filter based on multi-mode resonator," in *Proc. IEEE Int. Conf. Power Electron., Comput. Appl. (ICPECA)*, Shenyang, China, Jan. 2021, doi: 10.1109/ICPECA51329.2021.9362587.
[18] Y. Lin, M.-H. Weng, P. Zhang, and R.-Y. Yang, "A tri-band filter with controllable frequency and transmission zeros using dual-stubs loaded resonators," *Electromagnetics*, vol. 41, no. 2, pp. 131–141, Jan. 2021.
[19] L.-Q. Liu, Q.-Q. Yang, D.-L. Chen, M.-H. Weng, and R.-Y. Yang, "Design of tri-band bandpass filter using uniform impedance resonators loaded with different impedance stubs," *Electromagnetics*, vol. 41, pp. 253–262, May 2021.
[20] D. Li, Y. Zhou, S. Chen, and Y. Wu, "A compact tri-band bandpass filter using asymmetrical stub-loaded resonator," *Int. J. Electron.*, vol. 111, no. 1, pp. 170–183, Dec. 2022.
[21] S. Ding, J. Liang, X. Wang, C. Wang, N. Kim, and X. Gu, "A centrosymmetric-coupled tri-band bandpass filter constituted by loaded bar and embedded S-shaped resonator," *Microw. Opt. Technol. Lett.*, vol. 63, no. 11, pp. 2732–2739, Nov. 2021.
[22] F. Wei, H. J. Yue, X. H. Zhang, and X.-W. Shi, "A balanced quad-band BPF with independently controllable frequencies and high selectivity," *IEEE Access*, vol. 7, pp. 110316–110322, 2019.
[23] Y.-W. Chen, H.-W. Wu, Y.-W. Chen, R. Liu, H. Ye, and S.-K. Liu, "Design of new compact multi-layer quint-band bandpass filter," *IEEE Access*, vol. 9, pp. 139438–139445, 2021.

**XIAOHAN WAN** was born in Chengdu, Sichuan, China. She is currently pursuing the Engineering degree with Tianjin University of Technology, Tianjin, China. Her main research interests include bandpass filters and RF integrated circuits.

**ZHENGZHEN JIN** was born in Beijing, China. He is currently pursuing the Engineering degree with Tianjin University of Technology, Tianjin, China. His main research interests include the SVPWM and satellite navigation.

**YIFAN WANG** was born in Shaoyang, Hunan, China. She is currently pursuing the Engineering degree with Tianjin University of Technology, Tianjin, China. Her main research interest includes microwave filters.

**GUOXIN XU** was born in Zhengzhou, Henan, China, in 2003. He is currently pursuing the Engineering degree with Tianjin University of Technology, Tianjin, China. His main research interest includes the design of microwave tunable filters.

**LEI ZHANG** was born in Inner Mongolia Autonomous Region, China. She is currently pursuing the Engineering degree with Tianjin University of Technology, Tianjin, China. Her main research interest includes microwave differential filters.

**YANG XIONG** was born in Huaihua, Hunan, China, in 1990. He received the Ph.D. degree from Nankai University, Tianjin, China, in 2018. From 2018 to 2023, he was a Senior Engineer of microwave engineering with the Southwest China Institute of Electronic Technology, Chengdu, China. He is currently an Associate Professor with the School of Integrated Circuit Science and Engineering, Tianjin University of Technology, Tianjin. His research interests include microwave and millimeter-wave devices and integrated circuit designs.

**LITIAN WANG** was born in Tianjin, China, in 1991. He received the Ph.D. degree from Nankai University, Tianjin, in 2020. In 2020, he joined Tianjin University of Technology, Tianjin, where he is currently an Assistant Professor and the Deputy Director of the School of Integrated Circuit Science and Engineering. His current research interests include microwave passive devices and systems, high-temperature superconducting circuits, RF integrated circuits, and sensors.